A novel high voltage battery cathodes of Fe^{2+}/Fe^{3+} sodium fluoro sulfate lined with carbon nanotubes for stable sodium batteries

Ranjusha Rajagopalan
Sichuan University, University of Wollongong, ranjusha@uow.edu.au

Zhenguo Wu
Sichuan University

Yumei Liu
Sichuan University

Shaymaa Al-Rubaye
University of Wollongong, University of Babylon, shkar122@uowmail.edu.au

En-Hui Wang
Sichuan University, University of Wollongong

See next page for additional authors

Recommended Citation

A novel high voltage battery cathodes of Fe^{2+}/Fe^{3+} sodium fluoro sulfate lined with carbon nanotubes for stable sodium batteries

Abstract

Current trends in battery research are promoting the development of feasible methods to prepare electrode materials with new architectures that can meet the requirements of high energy density associated with sodium ion batteries (SIB). It is logical to use solid-state processing techniques to fabricate SIB electrode materials due to its ease of handling and capability for large-scale production. From the SIB standpoint, the sulfate based polyanionic system is well known for its high operating voltage. The present study utilizes a hitherto-unknown solid-state process with an entirely new composition to develop an electrode comprising earth abundant carbon, sodium, sulfur, fluorine, and iron materials. This new NaFeSO4F-CNT system, where CNT is carbon nanotube, obtained by the solid-state technique, exhibits a highly stable Fe2+/Fe3+redox couple and achieves a capacity of ~110 mAg−1at 0.1C with capacity retention of >91% after 200 cycles (1C). This is the best-ever reversible, high potential sulfate based cathode for sodium ion batteries reported to date. This study also provides an in-depth understanding of the outstanding electrochemical performance of this novel electrode. These findings can make it possible to achieve maximum performance from potential electrodes, when the operating temperature is limited to 350 °C or below.

Disciplines

Engineering | Physical Sciences and Mathematics

Publication Details

Authors

Ranjusha Rajagopalan, Zhenguo Wu, Yumei Liu, Shaymaa Al-Rubaye, En-Hui Wang, Chunjin Wu, Wei Xiang, Benhe Zhong, Xiaodong Guo, Shi Xue Dou, and Hua-Kun Liu

A novel high voltage battery cathodes of Fe^{2+}/Fe^{3+} sodium fluoro sulfate lined with carbon nanotubes for stable sodium batteries

Ranjusha Rajagopalan[1,2*], Zhenguo Wu[2], Yumei Liu[2], Shaymaa Al-Rubaye[1,3], Enhui Wang [1,2],

Chunjin Wu[2], Wei Xiang[2], Benhe Zhong[2], Xiaodong Guo[2*], Shi Xue Dou[1*], Hua Kun Liu[1*]

1. Institute for Superconducting and Electronic Materials, University of Wollongong, Wollongong, NSW 2522, Australia

Email: hua@uow.edu.au (Hua Kun Liu); shi@uow.edu.au (Shi Xue Dou); rranjusha@gmail.com, rr876@uowmail.edu.au (Ranjusha Rajagopalan)

2. College of Chemical Engineering, Sichuan University, Chengdu 610065, PR China.

Email: xiaodong2009@scu.edu.cn (Xiaodong Guo).

3. University of Babylon, College of education for pure sciences, Babylon, Iraq.

Abstract

Current trends in battery research are promoting the development of feasible methods to prepare electrode materials with new architectures that can meet the requirements of high energy density associated with sodium ion batteries (SIB). It is logical to use solid-state processing techniques to fabricate SIB electrode materials due to its ease of handling and capability for large-scale production. From the SIB standpoint, the sulfate based polyanionic system is well known for its high operating voltage. The present study utilizes a hitherto-unknown solid-state process with an entirely new composition to develop an electrode comprising earth abundant carbon, sodium, sulfur, fluorine, and iron materials. This new $NaFeSO_4F$-CNT system, where CNT is carbon nanotube, obtained by the solid-state technique, exhibits a highly stable Fe^{2+}/Fe^{3+} redox couple

and achieves a capacity of ~ 110 mAg^{-1} at 0.1C with capacity retention of > 91% after 200 cycles (1 C). This is the best-ever reversible, high potential sulfate based cathode for sodium ion batteries reported to date. This study also provides an in-depth understanding of the outstanding electrochemical performance of this novel electrode. These findings can make it possible to achieve maximum performance from potential electrodes, when the operating temperature is limited to 350°C or below.

Keywords: Sodium iron Fluoro Sulfate; carbon nanotubes; Fe^{2+}/Fe^{3+} redox couple; sodium-ion batteries; cycling.

1. Introduction

Increasing energy demands have directed the focus of researchers towards rechargeable energy devices with a good balance of capacity, power, cost, durability, and abundance of the necessary raw materials. Among them, lithium-ion batteries (LIBs) have become essential in everyday technology, with applications ranging from portable electronic devices to electric vehicles [1-3]. LiFePO$_4$ material with the Fe^{3+}/Fe^{2+} redox couple is considered to be the best commercialized material when considering its electrochemical performance in different applications. Nevertheless, these power sources are not suitable for grid-scale energy storage due to the high cost and low availability of lithium resources. For years, scientists have considered the sodium-ion battery (SIB) as a safer and lower cost replacement for LIBs in large-scale energy storage applications [4, 5]. The sodium chemistry per se has always been an exciting field of research, as it represents a perfect candidate to satisfy the most important requirements, such as abundance (with sodium the fifth most abundant element on Earth), accessibility, and worldwide distribution (and thus low cost) [6-9]. Thus, to benchmark against LiFePO$_4$, researchers have

broadened their range of exploration to search for new sodium based cathodes with a good mix of electrochemical properties and safety parameters. The natural tendency of the researchers was to replace the Li in the $LiFePO_4$ by Na. The operating voltage and associated energy density of its Na counterpart are inferior to those of lithium, however. Replacing the $(PO_4)^{3-}$ polyanion with the more electronegative $(SO_4)^{2-}$ can effectively utilize the improved operating voltage, and thus can solve the low energy density problem associated with the existing SIBs [10]. This approach was explored for a cathode material, $Na_2Fe_2(SO_4)_3$, which has a high Fe redox potential (~3.8 V) versus Na [2]. The study indicated that, in addition to possessing high redox potentials and promising Na^+ transport, these polyanion frameworks can exhibit good electrochemical stability, which makes them particularly suitable in applications where safety and longevity are important. Further, many similar studies have been conducted and have shown over 3 V operating potential and promising electrochemical properties (Table S1). Recently, fluorinated polyanion moieties (tavorite-type structured alkali metal fluoro-sulphate) have also received much attention [11-13]. The addition of fluoride promotes a charge difference and modification of the dimensionality of the lattice along with an altered redox potential. This framework possesses linear chains of corner-sharing FeO_4F_2 octahedra which propagate along the *c* axis and are bridged by corner-sharing SO_4 tetrahedra along the *a* and *b* axes to create a cavernous network, with two large intersecting tunnels for ion migration, which can house larger ions such as Na^+ and offer multidimensional pathways for ion transport [14, 15]. This ensures that good electrochemical performances can even be achieved with submicron particles, which provides significant advantages for material processing, and the opportunity for even faster ion transportation with lower path length. It seems, however, that the corresponding electrochemical performance cannot be improved as one would expect by ionic conductivity enhancement. For instance, these pristine

fluoro-sulphate polyanion compounds have the disadvantage of poor rate performance due to their low electronic conductivity. This problem is aggravated even more because of the sulfate compound in this material. The lower decomposition temperature of this sulfate limits the *in-situ* processing (using precursors) of conducting materials such as graphene, carbon nanotubes (CNTs), other conducting carbons, and/or cationic doping. Our experiences have shown that this is a major bottleneck in the processing of novel conducting fluoro-sulphate polyanion compounds for electrode applications. This could be one of the reasons why this class of materials has not been widely explored for battery electrodes.

The present study looks at this problem from two aspects: a) the development of a feasible and facile technique to prepare sodium-based fluoro-sulphate polyanion structures with optimal electrochemical properties and b) the improvement of its conductivity by employing carbon nanotubes (CNT) during the synthesis along with the precursor (to ensure intact and effective contact with the CNTs). The resultant structure is a new class of sodium iron fluoro-sulphate (hereby referred as SISF) lined by CNTs (SISF-CNT). As expected, the CNT lining over and around the SISF improved the conductivity of the sample, and it showed a specific capacity of ~110 mAh g^{-1} at 0.1 C. This functionally graded electrode benchmarks the highest-ever number of cycles (200 cycles) for the sulfate based Fe^{2+}/Fe^{3+} redox system at 1 C with > 91 % capacity retention.

2. Results and discussion

2.1. Phase characterizations of SISF and SISF-CNTs:

Even though SISF can exhibit a higher Fe^{2+}/Fe^{3+} redox potential than alternatives (Fig. S1 in the Supporting Information), the adoption of these cathodes in SIBs has been limited due to their

poor electronic conductivity and low processing temperatures. SISF undergoes a phase transformation above 350 $^{\circ}$C because of sulphate decomposition (Fig. 1a). This prevents the utilization of different carbon sources, such as oleic acid, glucose, and citric acid, to grow *in situ* in conducting carbon (Fig. S2) on SISF. Incomplete decomposition of these carbon sources results in low coulombic efficiencies and poor capacities of SISF (Fig. S2a-b). The present study employs a simple annealing technique wherein CNT is lined onto the SISF (detailed method provided in the Supporting Information). The amount of CNTs in the SISF matrix was optimized to 2.3 wt % (see Supporting Information method section and Fig. S3), and the sample with this percentage hence would be referred as SISF-CNT. Fig. 1b shows the X-ray diffraction (XRD) pattern of the pristine SISF and SISF-CNT samples. The patterns can be indexed to the monoclinic structure with space group of C2/c [12]. The crystal structure was refined using Rietveld refinement analysis. The refined XRD patterns and the corresponding crystal structure are shown in Fig. S4a-b. The lattice parameters and the reliability factors are reported in Table S2. The XRD pattern of CNT is presented in Fig. S5a. The 2 peaks observed in this pattern can be indexed to the (002) and (110) planes. The FTIR spectra (Fig. 1c) of SISF and SISF-CNT show the predominant overlapping vibration modes of $(SO_4)^{2-}$ in the range from 1400 to 700 cm^{-1}. The broad and prominent band around 1200−1050 cm^{-1} is assigned to the asymmetrical stretching of the tetrahedral SO_4^{2-}, while the peak located at 1004 cm^{-1} reflects the stretching vibration of SO_4^{2-}. The band at 3000-3600 cm^{-1} represents the vibration of OH groups [16, 17]. The Fourier transform infrared (FTIR) spectrum of CNT is shown in Fig. S5b. The identified peaks at 1116, 1637, 2919, and 3434 cm^{-1} represents different vibrations of C-O, C=C, C-H, and O=H bonds. The presence of additional peaks at 1510 cm^{-1} for SISF-CNT (Fig. 1d) as compared to pristine SISF (Fig. 1c) and in CNT (Fig. S4b) could be attributed to the C=C bonds in CNTs,

resulting from the linking of the oxygenated functional groups in the SISF [18]. The broadening

of the sulfate bands in SISF-CNT corresponds to the slightly different bonding of individual

sulfur molecules to the oxygen, resulting in infrared (IR) absorptions for each of these bonds at

various frequencies, which possibly occurred due to the lattice strain arising from the coefficient

of thermal expansion mismatch between the SISF and the CNT during the synthesis. Fig. 1d

shows the Raman spectra of SISF, CNT, and SISF-CNT samples. The absence of radial

breathing mode (RBM) bands indicates that the CNTs are multi-walled in nature [19]. There are

two characteristics bands, i.e. the G band (1578 cm^{-1}), representing the in-plane vibration of C–C

bonds along with a small shoulder band around 1605 cm^{-1}. The disorder induced D band also

appears at 1340 cm^{-1}. A harmonic of the D band is seen at 2680 cm^{-1}, called the G^{I} band [20].

The peaks below 1200 cm^{-1} represent different Raman vibration modes of SISF. X-ray

photoelectron spectroscopy (XPS) analysis (Fig. 1e) was carried out to understand the

conducting nature of the carbon and the purity of the SISF system. The peaks at

binding energies of 710 and 724 eV indicate the presence of Fe $2p_{3/2}$ and Fe $2p_{1/2}$ orbitals,

demonstrating the iron oxidation state in the SISF systems. The intense peak at 531 eV indicates

the presence of O 1s in the SO_4^{2-} group. The presence of Na could be observed by analyzing the

peaks at 1070, 62, and 30 eV. The S in the SO_4 can be observed through the peaks at 168 and

232 eV. At 684 eV, a sharp peak of F can also be observed. The C 1s peak at 284 eV was

deconvoluted to investigate the conducting nature of the carbon phase in the SISF-CNT system

(Fig. 1f). The 4 distinct deconvoluted peaks at 284.6, 285.8, 287.2, and 288.6 eV, represent the

C–C, C–O, C=O, and O–C=O bonds, respectively. The higher intensity of the C–C bonds as

compared to other bonds indicates the conducting nature of the carbon in the SISF-CNT system

through the delocalized π electrons. Compared to the pure CNT, blue shifts in the G, D, and G^{I}

bands in SISF-CNT were observed (Fig. 2a). Such shifts were absent in the case of the SISF bands (Fig. 2b), however. This could be accredited to the compressive strains experienced by the multi-walled CNTs from the SISF matrix [21]. In addition, a small increase in the peak intensity ratio (I_D/I_G) values for the SISF-CNT system (I_D/I_G = 1.069) was observed as compared to the pure CNT samples (I_D/I_G = 1.021). This larger value indicates the presence of disordered carbon atoms and/or the reduction of the crystallite size in the graphite domains of the CNT walls [22, 23]. The reason for this could be the damage induced on the CNT walls by the SISF matrix during the ball milling and/or during the thermal treatment. The Brunauer–Emmett–Teller (BET) analysis showed that the surface area of SISF-CNTs was more than 2 times greater (8 m^2g^{-1}) as compared to the pure SISF (3.5 m^2 g^{-1}). Also, the hysteresis observed between the adsorption and desorption curves in the BET isotherm of SISF-CNT indicates the presence of mesoporous structure in the material, while such hysteresis is absent in the pristine SISF system (Fig. S5c). Further, the isotherm of pure CNTs with a surface area of 113 m^2g^{-1} is provided in the inset of Fig. S5c.

2.2. Morphology analysis of SISF and SISF-CNTs:

Scanning electron microscope (SEM) images of SISF and SISF-CNT are shown in Fig. 3(a-c). The morphology of SISF shows a wide particle size distribution from the sub-micron to the micron scale (Fig. 3(a)). The morphology of SISF-CNT is shown in Fig. 3(b, c), where the active material particles with a size of 100-200 nm are effectively surrounded by CNTs, which not only acts as the bridges for continuous conductivity, but also act as barriers to prevent particle aggregation. An SEM image of the pure CNTs is provided in Fig. S6. In order to understand the arrangement of CNTs in the SISF-CNT sample, transmission electron microscopy (TEM) and

high resolution TEM (HRTEM) were carried out (Fig. 3d-h). Fig. 3d-e demonstrates the morphology of pure CNTs. The inner diameters of the CNTs are observed to range from 1.8 to 7.1 nm, while the wall thickness ranges from 1.7 to 5.9 nm. The selected area electron diffraction (SAED) pattern in the inset of Fig. 3d and the fast Fourier transform (FFT) pattern in the inset of Fig. 3e present bright electron diffraction spots in the Debye ring corresponding to the d spacing of 0.338 nm for the (002) lattice planes. Fig. 3 f-h presents TEM and HRTEM images of SISF-CNT. The inset of Fig. 3f shows the SAED pattern of the SISF-CNT system, where the electron diffraction pattern features bright spots for the SISF system along with the (002) plane Debye ring of CNT. The CNT network over the SISF particles can be observed in Fig. 3 g, h. To understand the interface between CNT and SISF better, 3 regions were selected, marked as 1, 2, and 3 in Fig. 3 h. Region 1 represents the CNT phase, while 2 and 3 cover different regions of the CNT lined SISF system. Further, the lattice fringes can be observed in the walls of these CNTs. The HRTEM images of these CNTs (shown in Fig. 4a) demonstrate clear lattice fringes with a d-spacing of ~0.338 nm, representing (002) planes. The corresponding FFT pattern (inset of Fig. 4a) shows bright diffraction spots in the Debye ring. The HRTEM image and the corresponding FFT pattern of the pristine SISF are shown in Fig. 4b and the inset of Fig. 4b, respectively. The corresponding FFT patterns are provided in Fig. 4c-e. The FFT pattern of region 1 in Fig. 3h (Fig. 4c) shows the d-spacing of 0.34, corresponding to the (002) planes of CNTs. The region 2 (in Fig. 3h) FFT pattern (Fig. 4d) features bright spots representing the SISF and the diffraction patterns of CNTs. The FFT pattern (Fig. 4e) of region 3 in Fig. 3h clearly shows CNT (002) planes along with the bright diffraction pattern of the SISF system. These FFT patterns, along with the HRTEM image, indicate that the CNTs are intact and well lined over the SISF, which could ensure faster Na migration and effective electron transportation.

2.3. Electrochemical performance evaluation of SISF and SISF-CNTs:

Fig. 5 shows the initial 5 cycles of charging-discharging (CD) at a rate of 0.1 C and the cyclic voltammetry (CV) curves for the first 5 cycles at the scan rate of 0.1 mV s^{-1} between 1.5–4.3 V (versus Na/Na^{+}) for the SISF and SISF-CNTs samples. Compared to SISF (Fig. 5 a, b), the SISF-CNT (Fig. 5 c, d) system showed distinct CD plateaus and CV redox peaks. The SISF-CNT sample showed an initial charge plateau at 3.7-3.9 V and a discharge plateau at 3.8-3.4 V. In the following cycles, the position of the charging plateau shifted towards lower voltage (3.6-3.8 V), while the discharging plateau remained the same (Fig. 5 c). This indicates the presence of some irreversible structural transformation during the first de-intercalation process. Thus, in the subsequent cycles, the voltage polarization appears to be smaller as compared to the first cycle, which, we believe, could provide better reversibility and electrochemical stability. In the case of the SISF sample, however, the phenomenon seems to be reversed (Fig. 5 a). In the CV curves, the shift in the redox peaks after the 1st cycle is not very evident, although the redox peaks are very prominent and in good agreement with the CD curves. For the SISF-CNT, apart from the main redox peaks, the CV analysis showed additional broad oxidation and reduction peaks at 3 and 2.8 V, respectively (Fig. 5d), but these redox peaks were absent in the pristine SISF system (Fig. 5b). Thus, the redox reaction associated with the Fe^{2+}/Fe^{3+} couple seems to occur in multiple stages. Also, in the CD curves, t2 voltage plateaus were observed in the SISF-CNT over the entire range, suggesting that 2 phase reaction mechanisms with different volume changes are associated with the reversible transformation of Fe^{2+} ↔ Fe^{3+}. The initial efficiency of SISF-CNT seems to be much better as compared to its pristine counterpart. The SISF-CNT showed an initial discharge capacity of ~110 mAhg^{-1} at 0.1 C, while SISF displayed only ~31 mAh g^{-1} at the same C rate.

Fig. 6a-b shows the electrochemical impedance spectroscopy (EIS) spectra of SISF and SISF-CNTs. The EIS analysis showed a significant reduction in the charge transfer resistance (R_{ct}) (Fig. 6a) and a minor reduction in the solution resistance (R_s) (Fig. 6b) for the SISF-CNTs as compared to the SISF. The R_s and R_{ct} values of the SISF and SISF-CNT samples are provided in Table S3. The inset of Fig. 6b shows the equivalent circuit of the SISF and SISF-CNT systems (where CPE is the constant phase element and W is the Warburg impedance). The reduction in the R_s and R_{ct} values of SISF-CNTs as compared to pristine SISF demonstrate its better ionic/electronic conductivity. To determine the effect of the CNT network on the diffusion, the diffusion coefficient has been calculated using the following equations.

$$Z' = R_s + R_{ct} + \sigma\omega^{-1/2} \tag{1}$$

$$D = \frac{R^2 T^2}{2A^2 n^4 F^4 C^2 \sigma^2} \tag{2}$$

where R_s is the solution resistance, R_{ct} is the charge transfer resistance, ω is the angular frequency at the low-frequency region, Z' is the real part of the impedance, and σ is the Warburg factor which is associated with Z' and ω. R is the gas constant, T is the absolute temperature, A is the surface area of the electrode, n is the number of the electrons per molecule during oxidization, F is the Faraday constant, and C is the concentration of sodium ion in the bulk.

To obtain the Warburg factor σ, the Z' vs $\omega^{-1/2}$ curve in the low frequency region is plotted, as is shown in Fig. S7. According to formulas (1) and (2), the calculated Na ion diffusion coefficients are presented in Table S3. The diffusion coefficient obtained for SIS-CNT is found to be one order of magnitude higher than for its pristine counterpart (Table S3). Based on the above analysis, rate capability studies of these two samples as

SIB cathodes, were also conducted in the potential window of 1.5-4.3 V (*vs.* Na$^+$/Na) to determine their practical electrochemical performance (Fig. 6c). A discharge capacity of ~110 mAhg^{-1} was obtained at a C rate of 0.1 C for the SISF-CNT electrode, and it could maintain a capacity over 85 mAhg^{-1} at 1 C. At 10 C, SISF-CNT electrodes could maintain a capacity of 30 mAhg^{-1} (which is equal to the capacity of pure the SISF system at 0.1 C) and recovered their initial capacity value after CD at different rates. Coulombic efficiency of more than 95% (Fig.6d) was consistently maintained at different C-rates. With a sudden change in the C rate, an unexpected decrease/increase in efficiency was observed, which could be attributed to the change in the participation of the active sites during the discharge process. The role of the CNTs in the SISF-CNT electrode is pivotal, as they could provide faster ion diffusion and a smoother path for the electrons during the CD processes. Here, the electrons can spread over the entire surface of SISF particles due to the presence of CNTs, leading to improved rate capability and reversibility of the sodium insertion/extraction cycles, as observed in the rate performance. The prime electron transport mechanism in CNTs depends on the network formed by the sp^2 bonded carbon atoms, which form long intact graphitic domains. The delocalized π-electrons are the principal reason for the better electronic conductivity of this form of carbon (as seen through the XPS analysis). The defect sites in the CNTs may hinder long-range electronic conductivity to some extent, but the sp^2 hybridized carbon domains form interacting pathways and provide smooth electron transportation, resulting in better electronic conductivity and a reduction in the net resistance, as observed in the EIS studies. Fig. 6e presents a cycling stability study of the SISF-CNT system at 1 C. The initial specific discharge capacity was found to be ~89 mAhg^{-1}. While the pristine SISF system showed

an initial specific capacity of ~13 mAh g^{-1} and it could only retain ~58% of its initial capacity at the end of 200 cycles (Fig. S8). Hence, it is worth noting that more than 91% of the capacity was retained for SISF-CNT system, even at the end of 200 cycles. The coulombic efficiency was observed to be more than 95% throughout the cycling process. This remarkable cycling stability could be attributed to the excellent structural stability of the SISF-CNT systems, even after the prolonged cycling. The CNT network could also minimize the stresses and loss in the electrode's structural integrity that are associated with the volume changes in the electrode during sodium intercalation/de-intercalation. In addition to this, the SISF structure, which is interconnected through CNTs, could be beneficial for the proper infiltration of the electrolyte. This would increase the liquid-phase sodium diffusion and eventually reduce the concentration polarization, resulting in better rate capability and capacity. The presence of CNTs in the SISF matrix can be advantageous for the following reasons: (a) the smaller un-agglomerated SISF particles can shorten the Na ion transportation length, as well as facilitating the reaction kinetics, (b) the CNTs lined over and around the SISF particles promote interfacial electrical conductivity and Na ion transfer, and (c) the CNT framework provides interconnected electron channels and helps the SISF structure to have a better accommodate volume changes.

Comparing the electrochemical performance of the present study with reports on different sodium iron sulphate materials (Table S1) [2, 24-29] shows that the present SISF-CNT system exhibits the best electrochemical performance to date, in terms of both capacity and stability. Nevertheless, there is further scope to improve the rate capability and energy density (Table S4) by devising new nanostructured architectures for SISF systems

or finding more suitable secondary phases. Also, it is very important to find out the percolation threshold limit and carryout a detailed conductivity study using a four-probe technique of the present system to explore the maximum electrochemical performance out of this system.

Conclusion

The present study opens up a new strategy for the development of high performance battery electrodes by means of a simple solid state technique, where the primary material can withstand only low processing temperatures. Based on this strategy, a novel CNT lined $NaFeSO_4F$ (SISF-CNT) system was fabricated and investigated for its electrochemical performance as a SIB cathode. The presence of the CNT network around SISF particles significantly improved the electrochemical performance as compared to pristine SISF. The microscopic and spectroscopic analysis revealed intimate contact between the SISF and the CNTs. The SISF-CNT cathode exhibited a discharge specific capacity of ~110 mAh g^{-1} with superior operating potential of ~3.6 V and promising cycling stability, with > 91% capacity retention after 200 cycles. Nevertheless, an appropriate active component for the counter electrode also needs detailed investigation in order to gain a deeper understanding of electrochemical performance of a full working cell. Furthermore, the high operating potential of ~3.6 V makes this system more attractive from a full cell standpoint.

References

[1] J. M. Tarascon, Is lithium the new gold? Nat. Chem. 2 (2010) 510.

[2] P. Barpanda, G. Oyama, S. Nishimura, S. C. Chung, A. Yamada, A 3.8-V earth-abundant sodium battery electrode, Nat. Commun. 5 (2014) 4358 1-8.

[3] A. K. Padhi, K. S. Nanjundaswamy, J. B. Goodenough, Phospho-olivines aspositive-electrode materials for rechargeable lithium batteries, J. Electrochem. Soc. 144 (1997) 1188–1194.

[4] X. Xiong, G. Wang, Y. Lin, Y. Wang, X. Ou, F. Zheng, C. Yang, J. H. Wang, M. Liu, Enhancing sodium ion battery performance by strongly binding nanostructured Sb_2S_3 on sulfur-doped graphene sheets, ACS Nano, 10 (2016) 10953–10959.

[5] J. M. Tarascon, Key challenges in future Li-battery research, Phil. Trans. R. Soc. A, 368 (2010) 3227-3241.

[6] S. Komaba, Electrochemical Na insertion and solid electrolyte interphase for hard-carbon electrodes and application to Na-ion batteries, Adv. Funct. Mater. 21 (2011) 3859–3867.

[7] C. Delmas, J. J. Braconnier, C. Fouassier, P. Hagenmuller, Electrochemical insertion of sodium in Na_xCoO_2 bronzes, Solid State Ion. 3–4 (1981) 165–169.

[8] Y. Zhong, X. Xia, J. Zhan, X. Wang, J. Tu, A CNT cocoon on sodium manganate nanotubes forming a core/branch cathode coupled with a helical carbon nanofibre anode for enhanced sodium ion batteries, J. Mater. Chem. A, 4 (2016) 11207-11213.

[9] Y.Wang, X. Xia, Y. Zhong, D. Zhou, D. Wang, X.Wang, J. Tu, Facile fabrication of integrated three-dimensional C-MoSe$_2$/reduced graphene oxide composite with enhanced performance for sodium storage, Nano Research, 9 (2016) 1618–1629.

[10] A. K. Padhi, K. S. Nanjundaswamy, C. Masquelier, J. B. Goodenough, Mapping of transition metal redox energies in phosphates with NASICON structure by lithium intercalation, J. Electrochem. Soc. 144 (1997) 2581–2586.

[11] P. Barpanda, J.N. Chotard, N. Recham, C. Delacourt, M. Ati, L. Dupont, M. Armand, Tarascon, J.M, Structural, transport, and electrochemical investigation of novel AMSO$_4$F (A = Na, Li; M = Fe, Co, Ni, Mn) metal fluorosulphates prepared using low temperature synthesis routes, Inorg. Chem. 49 (2010) 7401–7413.

[12] M. Reynauda, P. Barpanda, G. Roussec, J. N. Chotarda, B. C. Melota, N. Rechama, J. M. Tarascona, Synthesis and crystal chemistry of the NaMSO$_4$F family (M=Mg, Fe, Co, Cu, Zn), Solid State Sci. 14 (2012) 15-20.

[13] R. Tripathi, T. N. Ramesh, B. L. Ellis, L. F. Nazar, Scalable Synthesis of Tavorite LiFeSO$_4$F and NaFeSO$_4$F Cathode Materials, Angew. Chem. Int. Ed. 49 (2010) 8738 – 8742.

[14] R. Tripathi, G. R. Gardiner, M. S. Islam, L. F. Nazar, Alkali-ion Conduction Paths in LiFeSO$_4$F and NaFeSO$_4$F Tavorite-Type Cathode Materials, Chem. Mater. 23 (2011) 2278–2284.

[15] B. C. Melot, G. Rousse, J. N. Chotard, M. C. Kemei, J. R. Carvajal, J. M. Tarascon, Magnetic structure and properties of $NaFeSO_4F$ and $NaCoSO_4F$, Phys. Rev. B, 85 (2012) 094415 1-8.

[16] A. Sobkowiak, M. R. Roberts, R. Younesi, T. Ericsson, L. Häggström, C. W. Tai, A. M. Andersson, K. Edström, T. Gustafsson, F. Björefors, Understanding and controlling the surface chemistry of $LiFeSO_4F$ for an enhanced cathode functionality, Chem. Mater. 25 (2013) 3020−3029.

[17] X. M. Liu, S. L. Zhang, M. Yang, X. Z. Liao, H. Yang, X. D. Shena, Z. F. Ma, Synthesis and electrochemical evolution of mesoporous $LiFeSO_4F_{0.56}(OH)_{0.44}$ with high power and long cyclability, Chem. Commun. 50 (2014) 15247-15250.

[18] D. B. Mawhinney, V. Naumenko, A. Kuznetsova, J. T. Yates, J. Liu, R. E. Smalley, Infrared Spectral Evidence for the Etching of Carbon Nanotubes: Ozone Oxidation at 298 K, J. Am. Chem. Soc. 122 (2000) 2383-2384.

[19] A. I. L. Lorente, B. M. Simonet, M. Valcárcel, Raman spectroscopic characterization of single walled carbon nanotubes: influence of the sample aggregation state, Analyst, 139 (2014) 290-298.

[20] M. S. Dresselhaus, G. Dresselhaus, A. Jorio, A.G. S. Filho, R. Saito, Raman spectroscopy on isolated single wall carbon nanotubes, Carbon, 40 (2002) 2043–2061.

[21] G. Katumba, B. W. Mwakikunga, T. R. Mothibinyane, FTIR and Raman Spectroscopy of Carbon Nanoparticles in SiO_2, ZnO and NiO Matrices, Nanoscale Res. Lett. 3 (2008) 421–426.

[22] F. Tuinstra, J. L. Koenig, Raman Spectrum of Graphite, J. Chem. Phys. 53 (1970) 1126-1130.

[23] O. A. Maslova, M. R. Ammar, G. Guimbretiere, J. N. Rouzaud, P. Simon, Determination of crystallite size in polished graphitized carbon by Raman spectroscopy, Phys. Rev. B, 86 (2012) 134205 1-5.

[24] P. Barpanda, G. Oyama, C. D. Ling, A. Yamada, Kröhnkite-Type$Na_2Fe(SO_4)_2·2H_2O$ as a novel 3.25 V insertion compound for Na-ion batteries, Chem. Mater. 26 (2014) 1297−1299.

[25] Y. Meng, S. Zhang, C. Deng, Superior sodium–lithium intercalation and depressed moisture sensitivity of a hierarchical sandwich-type nanostructure for a graphene– sulfate composite: a case study on $Na_2Fe(SO_4)_2.2H_2O$, J. Mater. Chem. A, 3 (2015) 4484-4492.

[26] G. Oyama, S. Nishimura, Y. Suzuki, M. Okubo, A. Yamada, Off-Stoichiometry in Alluaudite-Type Sodium Iron Sulfate $Na_{2+2x}Fe_{2-x}(SO_4)_3$ as an Advanced Sodium Battery Cathode Material, ChemElectroChem. 2 (2015) 1019 – 1023.

[27] C. W. Mason, I. Gocheva, H. E. Hoster, D. Y. W. Yu, Iron(III) sulfate: A stable, cost effective electrode material for sodium ion batteries, Chem. Commun. 50 (2014) 2249-2251.

[28] P. Singh, K. Shiva, H. Celio, J. B. Goodenough, Eldfellite, $NaFe(SO_4)_2$: an intercalation cathode host for low-cost Na-ion batteries, Energy Environ. Sci. 8 (2015) 3000-3005.

[29] S. Wei, B. M. Boisse, G. Oyama, S. Nishimura, A. Yamada, Synthesis and Electrochemistry of $Na_{2.5}(Fe_{1-y}Mn_y)1.75(SO_4)_3$ Solid Solutions for Na-Ion Batteries, ChemElectroChem. 3 (2016) 209 – 213.

Figures Captions

Fig.1. a) XRD patterns of SISF annealed at different temperature, b) XRD patterns of SISF and SISF-CNTs, c) FTIR spectra of SISF and SISF-CNTs, d) Raman spectra of SISF, CNT, and SISF-CNTs, e) XPS spectra of SISF and SISF-CNTs, and f) deconvoluted C 1s spectrum of SISF-CNTs.
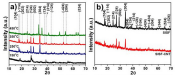
Fig. 2. Raman spectra showing the peak shifts of a) SISF-CNT and CNT, and b) SISF-CNT and SISF systems.
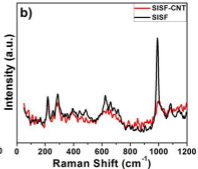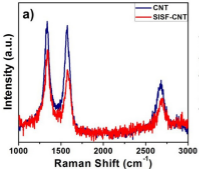
Fig.3. SEM images of a) SISF, b, c) SISF-CNT at different magnifications, d, e) TEM (inset: SAED pattern) and HRTEM (inset: FFT pattern) images of CNTs, f-h) TEM (inset: SAED pattern) and HRTEM images of SISF-CNTs.

Fig. 4. HRTEM images of a) CNTs and b) SISF system (insets: FFT patterns); FFT patterns of c) CNTs in region 1, d) CNT lined SISF in region 2, and e) CNT lined SISF in region 3 of Fig. 3h.
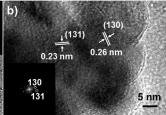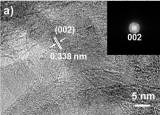
Fig. 5. a) charge-discharge curves, and b) CV curves of SISF; c) charge-discharge curves and d) CV curves of SISF-CNTs for the first 5 cycles.
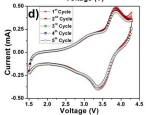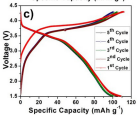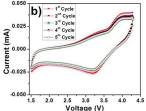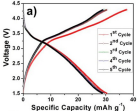
Fig. 6. a, b) EIS spectra (inset of Fig. 4b: equivalent circuit); c) rate performance and d) coulombic efficiency curves of SISF and SISF-CNTs; and e) cycling stability and coulombic efficiency curves of the SISF-CNT system at 1 C.
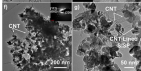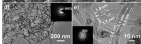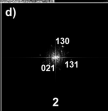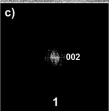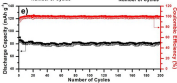
a)

b)

Figure with multiple electron microscopy panels (a–h) showing carbon nanotube (CNT) structures. Scale bars and labels visible include: 1 µm, 5 µm, 500 nm, 200 nm, 10 nm, CNT, CNT Lined SiSF, 50 nm, 0.34 nm, (111), 5 nm.

a) (002) 0.338 nm 002 5 nm

b) (131) 0.23 nm (130) 0.26 nm 130 131 5 nm

c) 002 **1**

d) 130 021 131 **2**

e) $\overline{3}12$ 221 130 131 112 002 **3**

A novel high voltage battery cathodes of Fe^{2+}/Fe^{3+} sodium fluoro sulfate lined with carbon nanotubes for stable sodium batteries

Ranjusha Rajagopalan[1,2*], Zhenguo Wu[2], Yumei Liu[2], Shaymaa Al-Rubaye[1,3], Enhui Wang [1,2], Chunjin Wu[2], Wei Xiang[2], Benhe Zhong[2], Xiaodong Guo[2*], Shi Xue Dou[1*], Hua Kun Liu[1*]

1. Institute for Superconducting and Electronic Materials, University of Wollongong, Wollongong, NSW 2522, Australia

Email: hua@uow.edu.au (Hua Kun Liu); shi@uow.edu.au (Shi Xue Dou); ranjusha@gmail.com, rr876@uowmail.edu.au (Ranjusha Rajagopalan)

2. College of Chemical Engineering, Sichuan University, Chengdu 610065, PR China.

Email: xiaodong2009@scu.edu.cn (Xiaodong Guo).

3. University of Babylon, College of education for pure sciences, Babylon ,Iraq.

Supporting Methods

Synthesis of NaFeSO₄F (SISF) and CNT lined SISF (SISF-CNT):

In a typical experiment, NaF and $FeSO_4$ in a stoichiometric ratio of 1:1 were mixed using a ball mill for 30 min. The resultant powder was kept for annealing at different temperatures, ranging from 150-450 ^0C for 12 h to obtain the SISF. To improve the conductivity of the sample, different amounts of CNTs were added as the carbon source prior to the ball milling and annealing. The optimized SISF sample covered in CNTs was designated as SISF-CNT, in which the weight percent of the carbon was found to be ~2.3 wt%. The optimization was conducted based on the charging-discharging performance of the electrodes at 0.1 C, and the carbon wt% was detected using the Carbon Hydrogen Nitrogen Sulphur analysis (CHNS) method (Figure S3).

Morphology and phase analyses of SISF and SISF-CNT:

The morphology of the SISF and SISF-CNT samples was observed using field emission scanning electron microscopy (SEM, SU3500 HITACHI) and high-resolution transmission electron microscopy (HRTEM) with energy dispersive spectroscopy (EDS) and selected area electron diffraction (SAED) (HR-TEM, ARM-200F, JEOL). Powder X-ray diffraction (XRD, XRD, D/max-rB, Rigaku, Japan, Cu Kα radiation), X-ray photoelectron spectroscopy (Kratos AXIS Ultra DVD, Kratos Analytical Lrd), Raman spectroscopy (Bio-Rad FTS6000, 532 nm blue laser beam), and Fourier transform infrared spectroscopy (FTIR; Bruker R200-L spectrophotometer) were used to determine the phases of the SISF and SISF-CNT samples. Rietveld refinement analysis was done with PDXL software. The carbon contents in the different SISF-CNT samples were examined using the CHNS (Carbon Sulphur Degerminator, CS-902C, Wanlianda Xinke) analysis. The specific surface area was obtained by using Brunauer-Emmett-Teller (BET, QDS-30) analysis.

Electrochemical characterization of SISF and SISF-CNT:

 In the half-cell preparation, the cathode was prepared with slurry consisting of 70 wt% active material, 20 wt% carbon black, and 10 wt% polyvinylidene fluoride (PVDF) binder dissolved in N-methyl pyrrolidone (NMP), which was then coated on Al foil and dried at 120 ^{0}C for 12 h. The coin cells (CR 2032) were assembled with pure Na foil as the counter and reference electrode. Glass fiber (GF/D, Whatman) and 1 M $NaClO_4$/propylene carbonate (PC) and ethylene carbonate (EC) (1/1, v/v) with 2% fluoroethylene carbonate (FEC) were used as separator and electrolyte, respectively. The cell assembly process was carried out in an Ar-filled

glove box, in which H_2O and O_2 were maintained at < 0.1 ppm. The assembled cells were galvanostatically analyzed using a multi-channel battery tester (Neware BTS-610) in the potential range of 1.5-4.3 V (vs. Na/Na^+) to obtain the capacity, rate performance, and cycling stability. Cyclic voltammetry (CV) studies at 0.1 mVs^{-1} scan rate were obtained using a LK9805 workstation, China. The electrochemical impedance spectroscopy (EIS) measurements in the frequency range from 1 MHz to 1 mHz were performed using a Zahner Z1.29 electrochemical workstation, with an applied amplitude of 5 mV.

Supporting Information Tables

Table S1: Electrochemical performance comparison of present system with different reported iron sulfate based polyanionic systems.

Electrode Material	Processing Technique	Carbon Form	C-rate	Capacity (mAh g^{-1})	No. of Cycles	Capacity Retention (%)	Voltage (V)	Reference No.
$Na_2Fe(SO_4)_2 \cdot 2H_2O$	Dissolution/ precipitation	Acetylene black	0.05	70	20	~80[*]	3.25	S1
$Na_2Fe(SO_4)_2 \cdot 2H_2O$	Low-temperature synthetic approach	Graphene	0.05	72	20	~94[*]	3.234	S2
$Na_{2-x}Fe_2(SO_4)_3$	Ball mill/ solid state technique	Ketjen Black	0.05	102	5	~98[*]	3.8	S3
$Na_{2+x}Fe_{2-x}(SO_4)_3$	Ball mill/solid state technique	-	0.05	100	-	70	3.05	S4
$Fe_2(SO_4)_3$	Ball mill technique	Super P	-	65	400	80	3.05	S5
$NaFe(SO_4)_2$	Solution route	Carbon black	0.05	~85[*]	80	~91*	3	S6
$Na_{2.5}(Fe_{1-y}Mn_y)_{1.75}(SO_4)_3$	Intermediate ball mill/ annealing	Acetylene black	0.05	~90[*]	-	-	3.8	S7
$NaFeSO_4F$	Ball mill/solid state technique	Super P /CNT	0.1	110	200	>91	3.6	Present study

*The values have been obtained from the graph.

Table S2: Crystallographic data of NaFeSO4F after the refinement of the crystal structure against the X-ray powder diffraction data at room temperature using the PDXL software.

Space group	C2/c
a (Å)	6.681(3)
b (Å)	8.714(4)
c (Å)	7.193(3)
α (deg.)	90.000
β (deg.)	113.54(2)
γ (deg.)	90.000
V (Å^3)	383.9(3)
Rwp (%)	5.18
Rp (%)	4.11
Re (%)	4.29
S	1.2071

X^2	1.4570	
Maximum Shift/e.s.d	0.084	

Table S3: Solution (R_s) and charge transfer (R_{ct}) resistances, and diffusion coefficient from the EIS curves.

	R_s (Ω)	R_{ct} (Ω)	Diffusion Coefficient: D (cm^2/s)
SISF	8.02	1272	2.65×10^{-17}
SISF-CNT	4.13	224	2.55×10^{-16}

Table S4: The theoretical and practical parameters of the SISF systems.

SISF	Capacity (mAh g^{-1})	Energy Density (Wh Kg^{-1})	Voltage (V)	Voltage polarization (mV)
Theoretical	~138	>520	>3.8	~0.03
Practically Achieved	110	~396	~3.6	~0.45

Supporting Information Figures
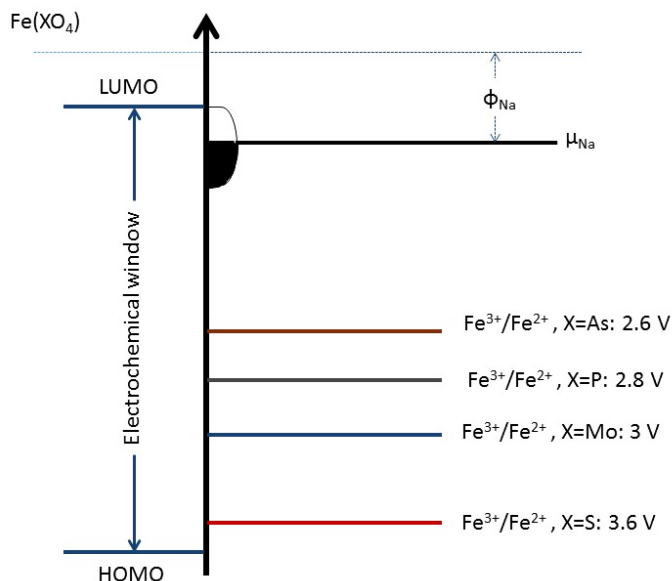
Fig. S1. Energy diagram showing the band positions of different polyanionic systems.

5
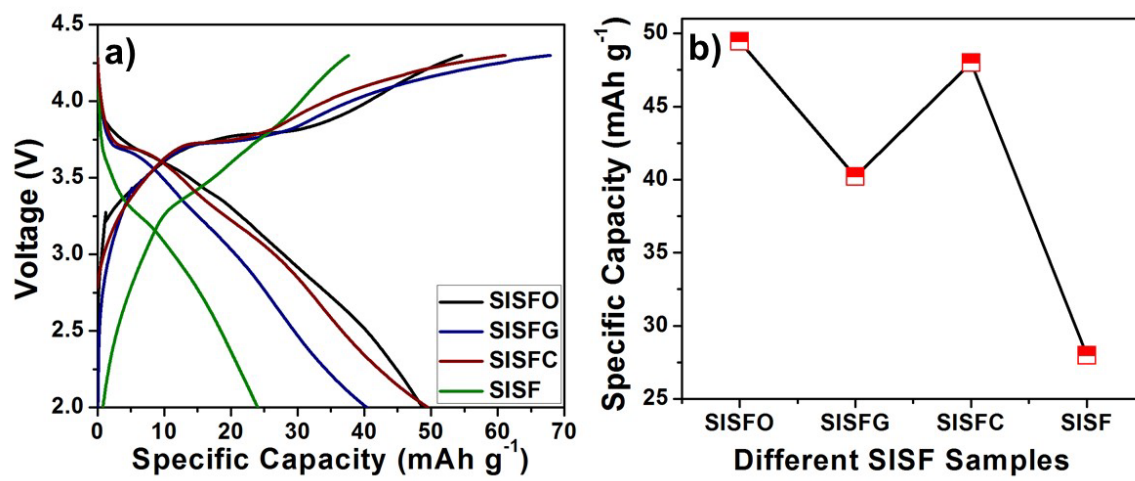
Fig. S2. a) Charge discharge curves of different carbon coated SISF samples (O: Oleic acid, G: Glucose, C: Citric acid derived carbon), and b) Specific capacity for SISF samples with different carbon coatings.
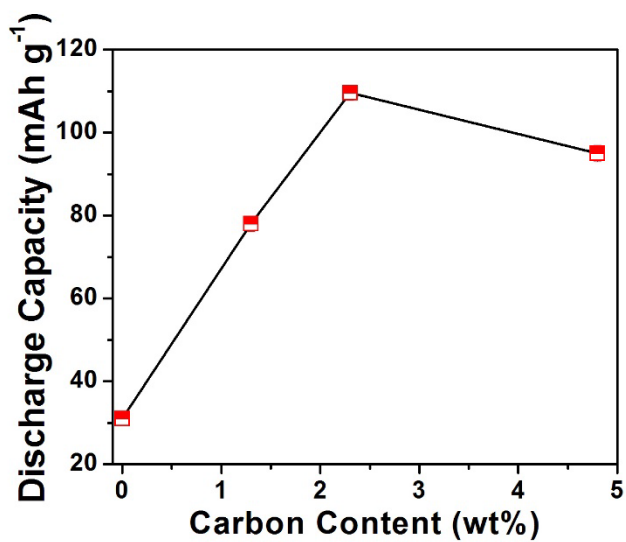

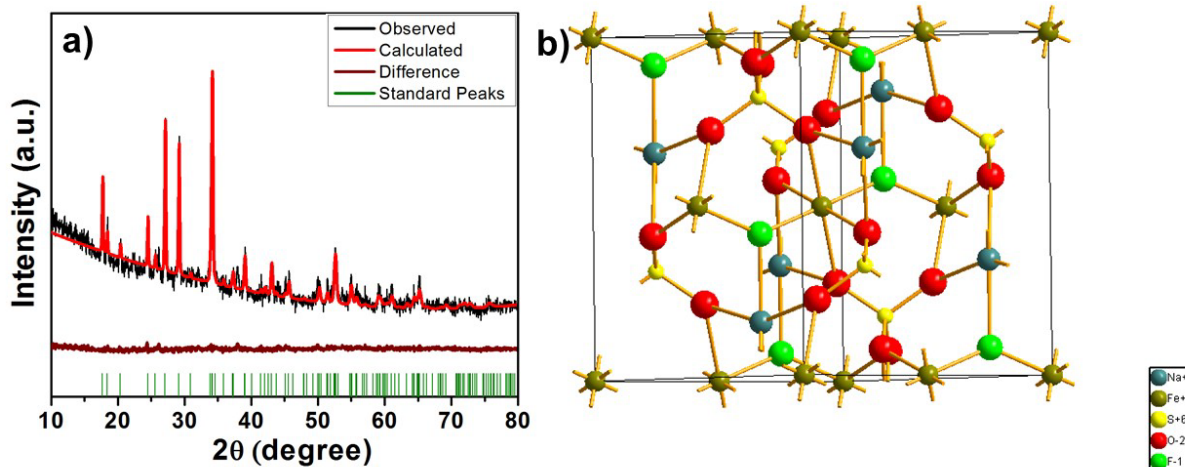Fig. S3. Capacity vs. Carbon content plot.

Fig. S4. a) Refined pattern using PDXL software, and b) corresponding crystal structure.
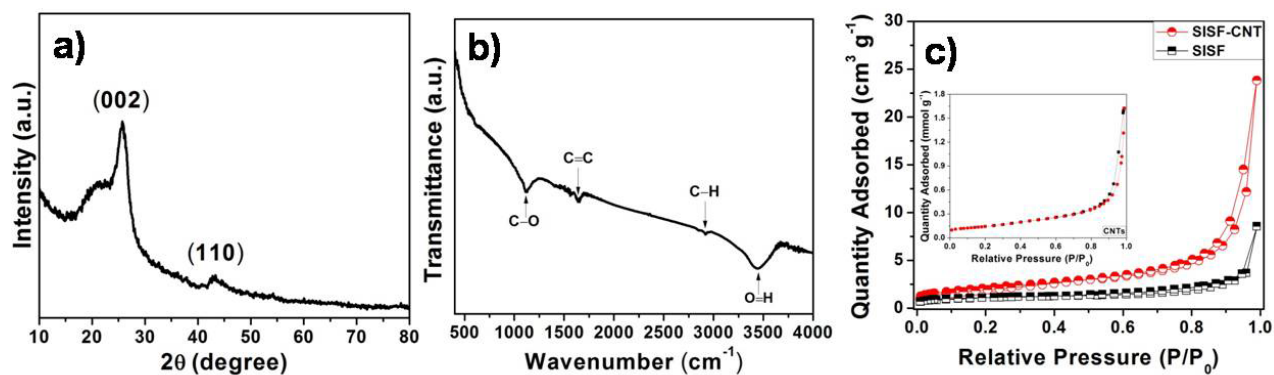

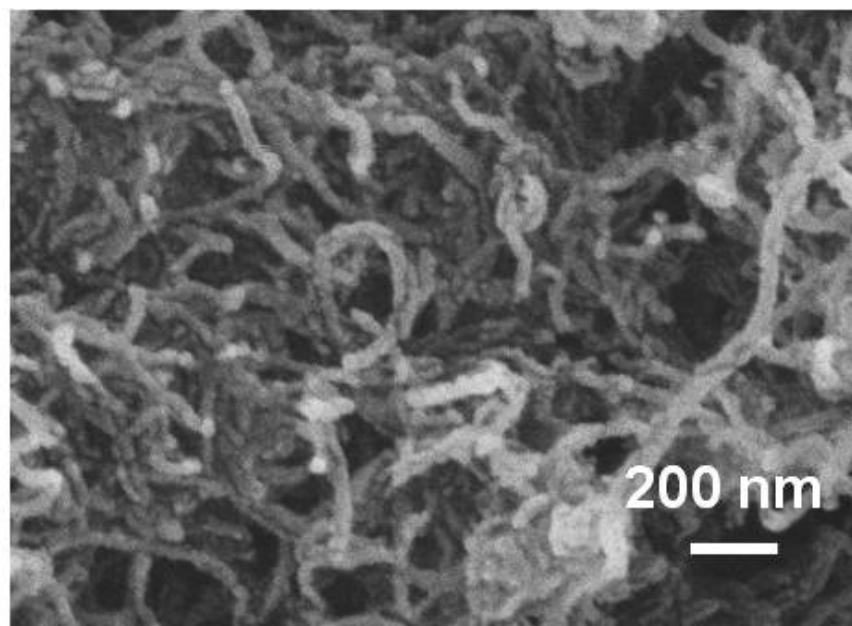Fig. S5. a) XRD pattern, b) FTIR spectrum of CNT and c) BET isotherms of SISF, SISF-CNT (inset CNTs).
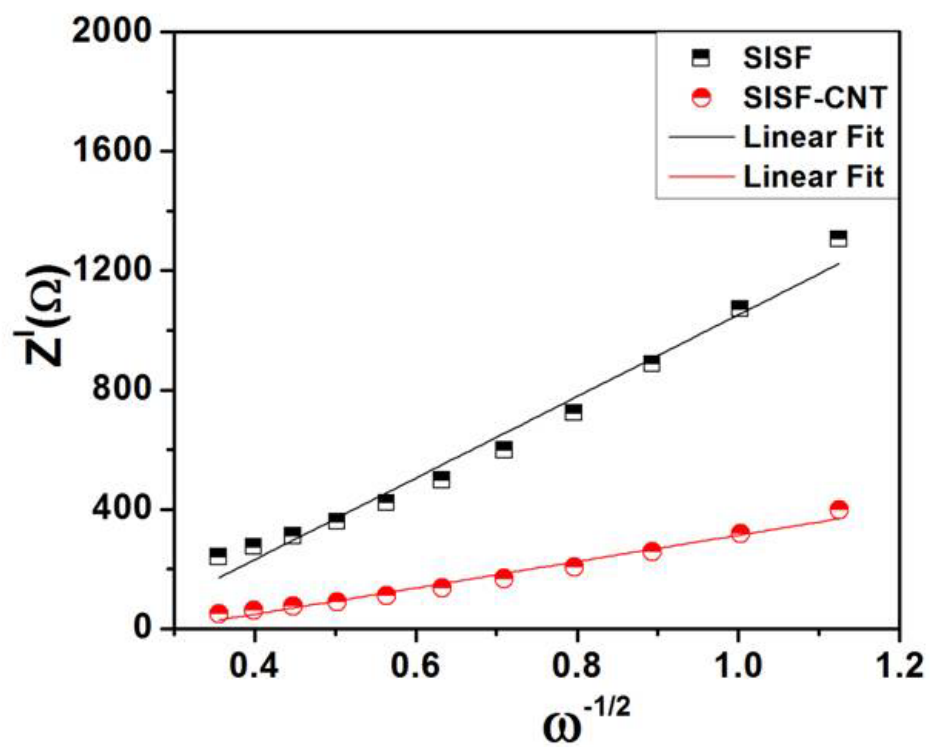
Fig. S6 SEM image of CNTs.

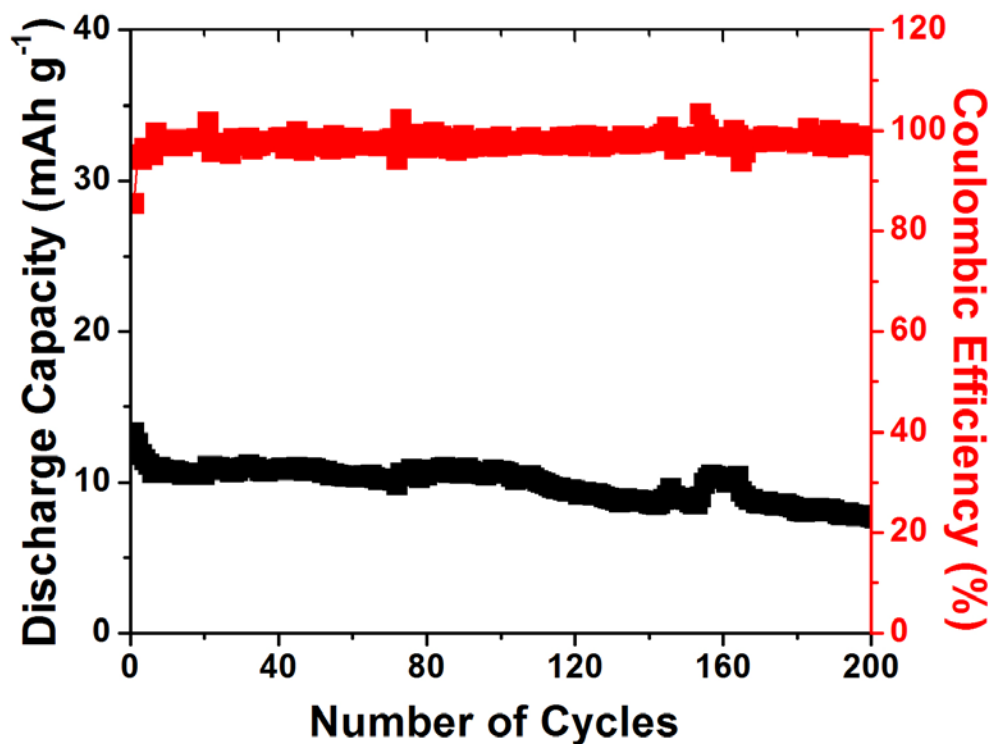Fig.S7. Impedance vs frequency curve.

Fig.S7. Cycling stability curve of pristine SISF sample.

References

S1. P. Barpanda, G. Oyama, C. D. Ling, A. Yamada, Kröhnkite-TypeNa$_2$Fe(SO$_4$)$_2$·2H$_2$O as a novel 3.25 V insertion compound for Na-ion batteries, Chem. Mater. 26 (2014) 1297−1299.

S2. Y. Meng, S. Zhang, C. Deng, Superior sodium–lithium intercalation and depressed moisture sensitivity of a hierarchical sandwich-type nanostructure for a graphene– sulfate composite: a case study on Na$_2$Fe(SO$_4$)$_2$.2H$_2$O, J. Mater. Chem. A, 3 (2015) 4484-4492.

S3. P. Barpanda, G. Oyama, S. Nishimura, S. C. Chung, A. Yamada, A 3.8-V earth-abundant sodium battery electrode, Nat. Commun. 5 (2014) 4358 1-8.

S4. G. Oyama, S. Nishimura, Y. Suzuki, M. Okubo, A. Yamada, Off-Stoichiometry in Alluaudite-Type Sodium Iron Sulfate $Na_{2+2x}Fe_{2-x}(SO_4)_3$ as an Advanced Sodium Battery Cathode Material, ChemElectroChem. 2 (2015) 1019 – 1023.

S5. C. W. Mason, I. Gocheva, H. E. Hoster, D. Y. W. Yu, Iron(III) sulfate: A stable, cost effective electrode material for sodium ion batteries, Chem. Commun. 50 (2014) 2249-2251.

S6. P. Singh, K. Shiva, H. Celio, J. B. Goodenough, Eldfellite, $NaFe(SO_4)_2$: an intercalation cathode host for low-cost Na-ion batteries, Energy Environ. Sci. 8 (2015) 3000-3005.

S7. S. Wei, B. M. Boisse, G. Oyama, S. Nishimura, A. Yamada, Synthesis and Electrochemistry of $Na_{2.5}(Fe_{1-y}Mn_y)1.75(SO_4)_3$ Solid Solutions for Na-Ion Batteries, ChemElectroChem. 3 (2016) 209 – 213.